Promoting the photocatalytic NO oxidation activity of hierarchical porous g-C$_3$N$_4$ by introduction of nitrogen vacancies and charge channels

Yang Xia [a,c], Heng Yang [e], Wingkei Ho [a,d,*], Bicheng Zhu [b], Jiaguo Yu [b,**]

[a] Department of Science and Environmental Studies and the Centre for Environment and Sustainable Development (CESD), The Education University of Hong Kong, Tai Po, New Territories 999077, Hong Kong, China
[b] Laboratory of Solar Fuel, Faculty of Materials Science and Chemistry China University of Geosciences, Wuhan 430074, PR China
[c] Key Laboratory of Green Chemical Process of Ministry of Education, School of Chemical Engineering and Pharmacy, Wuhan Institute of Technology, Wuhan 430205, PR China
[d] State Key Laboratory of Marine Pollution, City University of Hong Kong, Tat Chee Avenue, Kowloon, Hong Kong, China
[e] College of Chemistry and Environmental Engineering, Wuhan Polytechnic University, Wuhan 430023, PR China

A R T I C L E   I N F O

A B S T R A C T

Sluggish charge kinetics and moderate adsorption–desorption ability of gas molecules are major limitations for photocatalytic NOx elimination of bulk g-C$_3$N$_4$. A hierarchical porous g-C$_3$N$_4$ photocatalyst modified with N vacancies and charge channels (KCNN) was prepared by thermal polymerisation in KCl medium followed by quenching to increase the photocatalytic efficiency. The optimized KCNN sample exhibits highly enhanced photocatalytic NO removal rate (70.5%), which is superior to those of bulk g-C$_3$N$_4$ (38.1%), porous g-C$_3$N$_4$ (54.5%) and K-doped g-C$_3$N$_4$ (58.6%), respectively. X-ray photoelectron spectroscopy and electron paramagnetic resonance data reveal the successful formation of N vacancy in g-C$_3$N$_4$ framework. The enhanced activity of KCNN is ascribed to the enlarged surface area, expanded light absorption, low charge recombination efficiency and strong oxidation capability, respectively. In situ DRIFTS and density functional theory results suggest that the introduction of N vacancies and K$^+$ ions enable control over NO adsorption and activation, leading to the implementation of a preferred pathway (NO $\rightarrow$ NO$^+$ $\rightarrow$ NO$_3^-$) and reduction in the emission of toxic intermediates. This work presents a potential idea for improving the charge transfer of layered materials and optimising the diffusion/adsorption/activation of gas molecules for photocatalytic NO oxidation.

1. Introduction

Environmental pollution caused by the industrialisation and rapid development of the society has become an enormous challenge for the sustainable future of humans [1–5]. Nitrogen oxide (NOx) generated from coal-fired combustion and automobile exhaust has severe effects on air quality and causes respiratory diseases [6–8], thereby destroying the ecological balance and posing a threat to public health. Therefore, the removal of NOx in air has become the goal in the past few years. Many strategies, such as physical absorption [9,10], plasma treatment [11,12], selective catalyst reduction [13,14] and so on, have been utilised for NOx removal. However, they not only suffer from the consumption of depletable resources but also bring about the risks of secondary pollution. Therefore, a suitable and green method should be

developed for NOx removal in air. Compared with the above strategies, photocatalytic technology exhibits great potential to remove atmospheric NO owing to its low cost, environment friendliness and efficient properties [15–17]. In photocatalysis, the basic and prerequisite of NO oxidation are to explore and synthesise highly active photocatalysts.

A variety of semiconductor photocatalysts (TiO$_2$ [18,19], g-C$_3$N$_4$ [20,21], Bi-based materials [22,23], SrTiO$_3$ [24,25], etc.) have been developed for photocatalytic air purification. Thereinto, graphitic carbon nitride (g-C$_3$N$_4$) has been considered one of the most advantageous materials for photocatalytic NO removal due to its easy preparation, non-toxicity, suitable bandgap, high chemical stability and abundant reserves [26,27]. Nevertheless, the photocatalytic NO oxidation performance of bulk g-C$_3$N$_4$ is far from ideal because it has low crystallinity, insufficient utilisation of sunlight and rapid recombination of charge

carriers. Thus, tremendous efforts have been made to enhance catalytic performance by heteroatom doping [28], constructing heterojunction [29], cocatalyst loading [30], morphological control [31], vacancy engineering [32] and nanostructure design [33]. Among them, the introduction of heteroatoms into the structure of g-C$_3$N$_4$ is an effective strategy for promoting photocatalytic activity because it changes the electron distribution, band gap and light response region of g-C$_3$N$_4$. Alkali metal K atom doping not only expands the visible-light response range, modulates redox band potentials and accelerates photogenerated charge carrier separation, but also induces the generation of multiple active units. Nevertheless, alkali metal-doped g-C$_3$N$_4$ is inclined to aggregate during polymerisation owing to inevitable adhesion induced by strong van der Waals force between layers and the insertion effect of metal atoms. The design of hierarchical porous g-C$_3$N$_4$ nanosheet structure can efficiently suppress aggregation and enhance photocatalytic performance because of its higher specific surface area, excellent light absorption and fast mass transport. Many studies have fabricated this ideal structure through template-assisted strategy and additive agent-mediated strategy [34,35]. These methods can introduce vacancies or defects into the g-C$_3$N$_4$ framework to modify the band structure by generating additional energy level in the band gap and serve as trapping sites for photoinduced charge carriers to suppress their recombination. However, these routes are complicated and time consuming and require extensive energy. Therefore, developing a green and facile strategy for constructing hierarchical porous g-C$_3$N$_4$ nanosheet structure with vacancy is of critical importance.

Taking the above consideration, alkali metal K atom doping and construction of hierarchical porous structure with vacancies are synchronously achieved in the tri-s-triazine repeating units of g-C$_3$N$_4$ by a green route. A result of 'win-win' will be obtained while improving photocatalytic NO oxidation by using the designed photocatalyst. Herein, hierarchical porous kalium-doped g-C$_3$N$_4$ nanosheets with N vacancies were prepared through thermal polymerisation followed by liquid N$_2$ quenching. The obtained material exhibits high photocatalytic performance towards NO removal. The effects of such modifications on the photoelectric properties and electron conductivity of g-C$_3$N$_4$ were systematically investigated through experiments combined with theoretical calculations. The photocatalytic NO removal mechanism was also elucidated through in situ diffuse reflectance infrared Fourier transform (DRIFTS) analysis. This work could bring new perspectives to design novel and highly efficient g-C$_3$N$_4$-based materials for safe NOx purification in air.

2. Experimental section

2.1. Materials

Urea was purchased from Sinopharm Chemical Reagent Co., Ltd. (Shanghai, China). Potassium chloride was obtained from Bodi Chemical Engineering Co., Ltd. (Tianjin, China). All the chemicals were of analytical grade and used as received without further treatment.

2.2. Synthesis and characterisation

g-C$_3$N$_4$ and K-doped g-C$_3$N$_4$ were prepared by facile thermal polycondensation. Hierarchical porous g-C$_3$N$_4$ and hierarchical porous K-doped g-C$_3$N$_4$ were synthesised by simple thermal polycondensation and quenching into liquid nitrogen. Detailed experimental process and characterisation techniques are provided in Electronic Supplementary Information.

### 2.3. Photocatalytic activity measurement

The photocatalytic activity of the as-prepared samples was evaluated in a continuous-flow reactor through the photodegradation of NO at the parts per billion (ppb) level. Typically, the catalyst (0.1 g) was uniformly

dispersed into 30 mL of water under ultrasonication for 10 min. The suspension was transferred and smeared on a glass dish with a diameter of 11.5 cm and heated at 60 °C on a heater to completely evaporate the water from the suspension. After cooling down to room temperature, the dish with the sample film was placed in the reaction chamber. Before irradiation by 30 W LED lamp with LOPB-30D model (SUNSHINE Light Company, Hong Kong, China), NO gas was mixed with O$_2$ in a reactor with the humidity of about 50%, while flow rate was controlled by a mass flow controller. After the adsorption–desorption equilibrium of NO (about 500 ppb) was achieved, the LED lamp was turned on to trigger the photocatalytic reaction (the temperature of the reaction system was kept at 25 °C). NO concentration was monitored using a chemiluminescence NO$_x$ analyser (Advanced Pollution Instrumentation, Teledyne Technologies, Model T200). The removal ratio (η) of NO was calculated as η (%) = (1-C/C$_0$) × 100, where C and C$_0$ are the concentrations of NO in the outlet and initial feeding streams, respectively.

3. Results and discussion

Hierarchical porous K-doped g-C$_3$N$_4$ was synthesised by simple thermal polycondensation and quenching into liquid nitrogen. As shown in Fig. 1a, the mixture of urea and KCl salt was placed in an alumina crucible and calcined at 600 °C in a muffle furnace for 3 h. The high-temperature melt was quenched into liquid nitrogen. Washing and vacuum drying were conducted to collect fine powder, which was denoted as KCNN. For comparison, other samples (CN, CNN and KCN) were prepared by adopting the same heating condition but cooled in a furnace or without adding KCl salt. The detailed methodology could be found in the Experimental section. The morphology and microstructure of the as-prepared samples were investigated by field-emission scanning electron microscopy (FESEM) and transmission electron microscopy (TEM). As shown in Fig. 1b, CN presented a tightly stacked plate structure. After cold quenching by liquid nitrogen, the obtained sample of CNN featured a hierarchical porous structure with a curling edge (Fig. 1c). The KCN sample, which was obtained through thermal polymerisation of urea and KCl salt and subsequent air cooling, retained the thin section structure and a part of them became tighter (Fig. 1d); this special morphology could be due to the strong interactions between g-C$_3$N$_4$ layers and the doped K ions [36]. The KCNN sample featured fluffy and porous ultrathin nanosheets with a folded edge (Fig. 1e), which markedly differed from the structure of the KCN sample. The change in morphology and microstructure could be attributed to the warping effect of K atoms and the quenching-induced effect of liquid nitrogen on the layer of g-C$_3$N$_4$ [37,38]. The microstructures of the as-prepared samples were furtherly investigated by TEM. As shown in Figs. S1 and 1f-g, CN displayed a layered structure composed of irregular stacks of two-dimensional nanosheets (Fig. 1f), while CNN presented loosely interconnected nanosheets with a porous structure (Fig. S1a). The KCN sample exhibited a stacked plate agglomerate structure, which was difficult to exfoliate probably due to the interactions between g-C$_3$N$_4$ layers and doped K$^+$ ions (Fig. S1b). After K$^+$ ion doping and cold quenching, the obtained KCNN samples showed hierarchical porous nanosheets, and a part of them became more creased (Fig. 1g). Moreover, high-resolution TEM (HRTEM) further revealed the structure and composition. Fig. 1h exhibited clear lattice fringes with lattice spacing of about 0.336 nm, corresponding to the heptazine π-π layer stacking (002) plane of KCNN. Meanwhile, high-angle annular dark-field scanning transmission electron microscopy (HAADF-STEM) and its elemental mapping of energy-dispersive X-ray spectroscopy (EDS) show the uniform distribution of C, N, K and O elements in KCNN (Fig. 1i). Therefore, these results indicated that cold quenching and K$^+$ ion doping were important for constructing interconnected porous structures comprising nanosheets and increasing the crystallinity of g-C$_3$N$_4$.

The crystal structures of the as-prepared samples were detected by X-ray diffraction (XRD) patterns. As shown in Fig. 2a, two characteristic peaks of the CN sample were observed at 13.2° and 27.3° corresponding
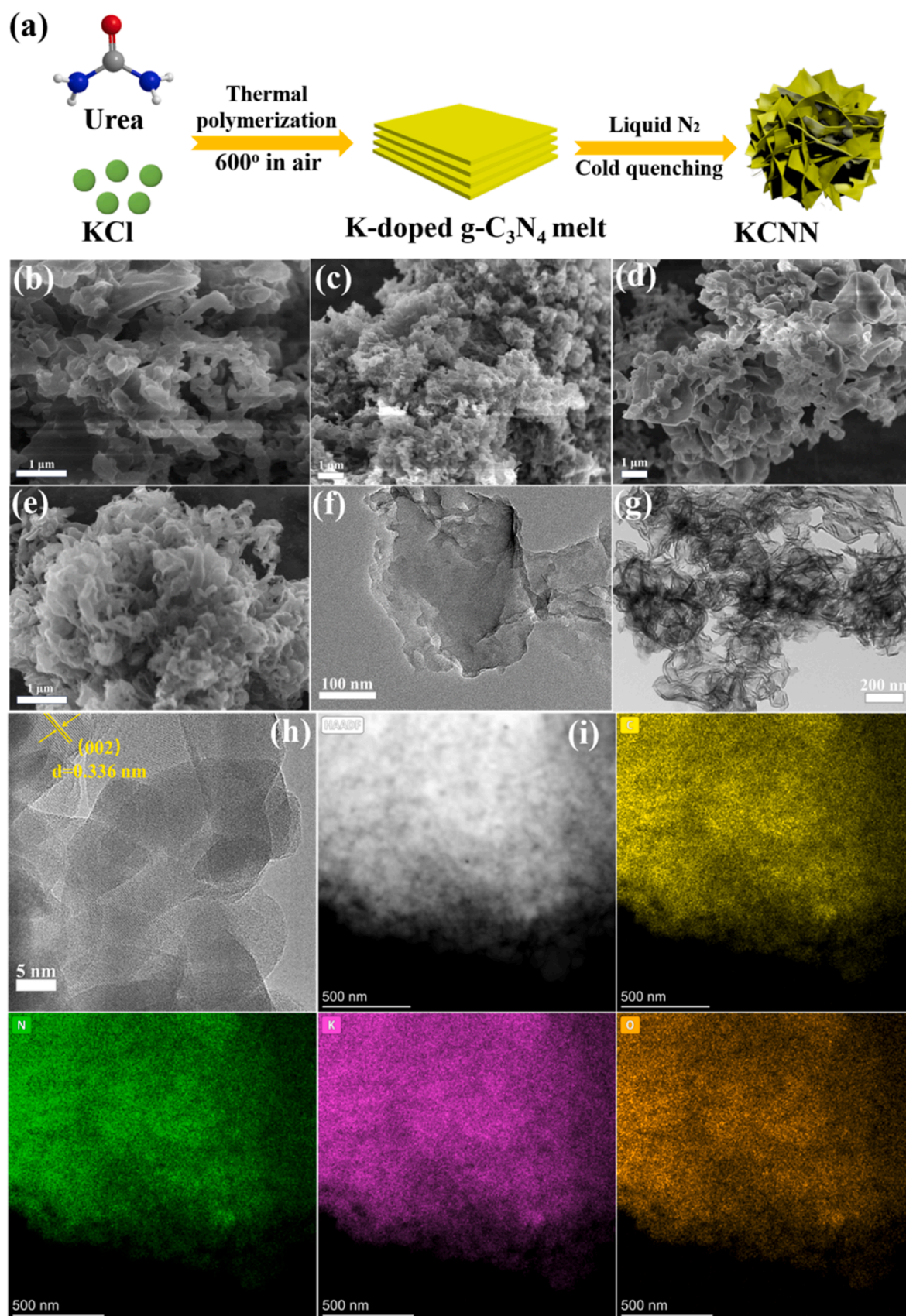
Fig. 1. (a) Schematic of the experimental process of KCNN; FESEM images of (b) CN, (c) CNN, (d) KCN and (e) KCNN. TEM images of (f) CN and (g) KCNN. (h) HRTEM image and (i) HAADF-STEM image of KCNN and corresponding elemental mapping image of C, N, K and O.
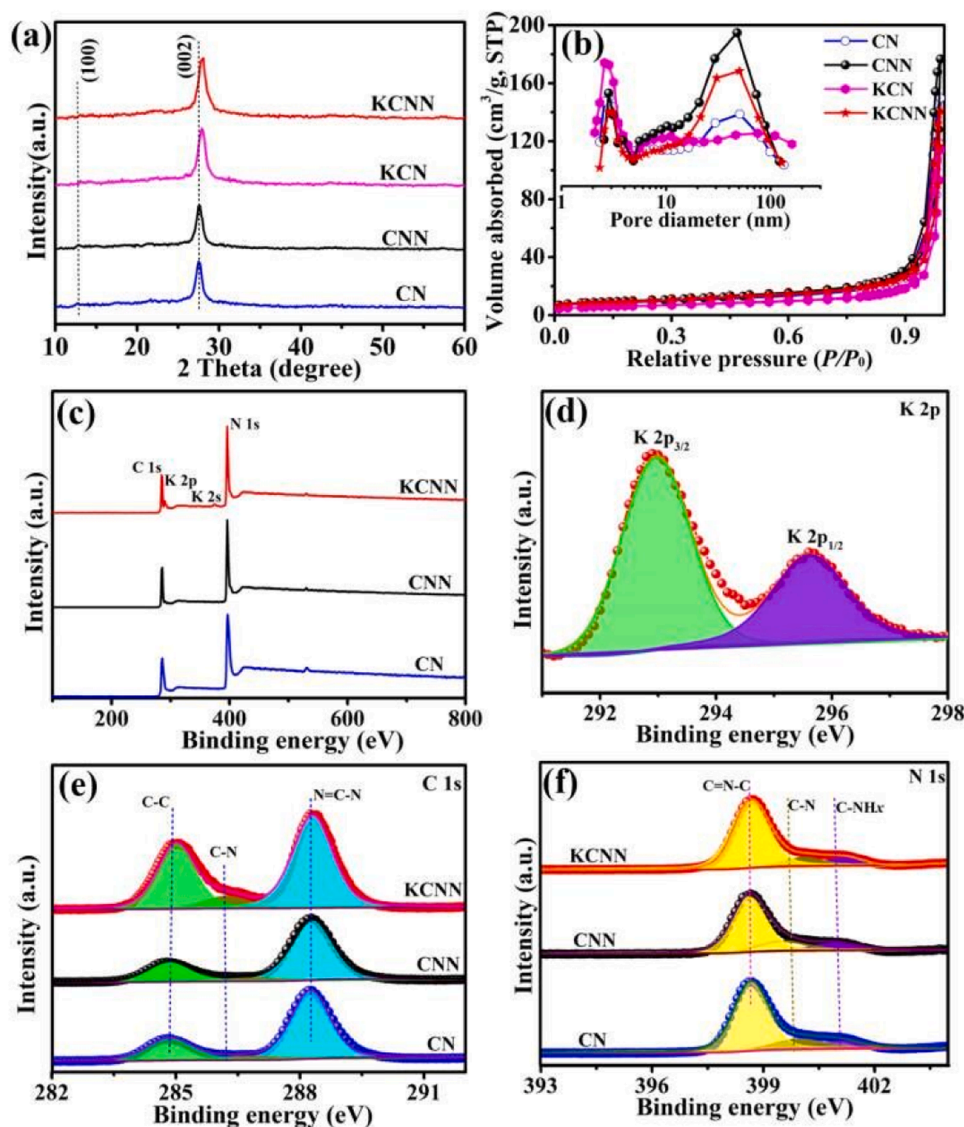
Fig. 2. (a) XRD patterns and (b) N$_2$ adsorption–desorption isotherms and pore distribution curves of CN, CNN, KCN and KCNN. (c) XPS survey spectra of CN, CNN and KCNN. (d) High-resolution XPS spectrum of K 2p in KCNN. High-resolution XPS spectra of (e) C 1 s and (f) N 1 s in CN, CNN and KCNN samples.

to the (100) facet and (002) facet, which could be assigned to the in-plane structural repeating motifs of the aromatic systems and the interlayer stacking, respectively [39–41]. The CNN, KCN and KCNN samples revealed similar features to that of CN. However, the intensity of the two diffraction peaks over them became stronger compared with that of CN. The (002) plane right-shifted from 27.3° for CN and CNN to 27.8° for KCN and KCNN, suggesting that the introduction of KCl improved the crystallinity and decreased the interlayer distances between two adjacent unit layers of g-C$_3$N$_4$. The molecular structures of the as-prepared samples were further analysed by FT-IR spectroscopy. Fig. S2 shows the FT-IR spectra of CN, CNN, KCN and KCNN samples. The peaks located at 810 and 887 cm^{-1} were attributed to the stretching vibration of triazine units and the N-H deformation of the triazine unit, respectively [42]. The peaks centred at 1250 and 1640 cm^{-1} were ascribed to -C≡N heterocycles [43]. In addition, a broad absorption peak between 3000 and 3500 cm^{-1} was associated with N–H bonds, O–H bonds and water molecules [44]. After the introduction of KCl salt, four obvious changes emerged in the FT-IR spectra of KCN and KCNN. Firstly, a distinct peak emerged at 2175 cm^{-1}, which could be related to the cyano group. Secondly, the signal peak intensity of $-C-NH_2$ decreased progressively in relation to the cyano group. Thirdly, the

intensity of the triazine ring peak centred at 810 cm^{-1} decreased. Finally, the peak intensity of N-H deformation mode in amino groups at 887 cm^{-1} gradually became weaker. These changes suggest that the K$^+$ ions inserted into the heptazine of g-C$_3$N$_4$, causing structural distortion and the increase of cyano groups. Moreover, to reveal the effects of K$^+$ ion and liquid nitrogen treatment on the surface area and porosity of the as-prepared samples, the nitrogen adsorption was carried out to evaluate the Brunauer–Emmett–Teller (BET) specific surface area and porous structure. As illustrated in Fig. 2b, the N$_2$ adsorption–desorption isotherms of all the as-prepared samples were typical type IV isotherms and H3-hysteresis loop ($0.7 < P/P_0 < 1.0$) [45,46], suggesting that mesopores and macropores coexisted in all the obtained samples. It was noteworthy that the specific surface areas of CNN and KCNN were larger than those of CN and KCN (Table S1), which could be ascribed to the cold quenching effect of liquid nitrogen. The specific surface area of KCN was smaller than that of CN. The reduction in the surface area of KCN could be due to KCl, which restricted the release of NH$_3$ and CO$_2$ gas during thermal polycondensation [47]. In addition, the pore size distribution plots of the as-prepared samples are shown in the inset of Fig. 2b. The pore diameters of CN, CNN and KCNN were mainly distributed at about 3.0 and 60 nm, suggesting the dominance of

mesopores and macropores. By contrast, KCN exhibited a wide distribution of pore size in the range of 2–100 nm and a main distribution centre located at 3 nm, demonstrating that the mesopore structure was dominant in KCN. It was important note that the pore volumes of macropore in CNN and KCNN increased compared with that of CN. This finding could be attributed to the transformation of CN nanosheets into a hierarchical structure. Upon K^+ ion doping, the pore volumes of mesopores/macropores decreased compared with that of CN due to the interaction of urea with metals. Hence, the insertion of K atoms could decrease interlayer distances, resulting in reduced specific surface areas. The quenching treatment of liquid nitrogen on CN could produce larger size holes, thereby increasing the special surface area and average pore size.

X-ray photoelectron spectroscopy (XPS) measurement was performed to further reveal the chemical composition and states of the as-prepared samples. As shown in Fig. 2c, the XPS survey spectra confirm the presence of C, N and O in CN, CNN and KCNN samples, while K element could be found in KCNN. The high-resolution K 2p spectrum of KCNN presented two peaks at 295.4 ($K 2p_{1/2}$) and 292.8 eV ($K 2p_{3/2}$) (Fig. 2d), which correspond the binding energy of the K-N bond and indicated the presence of K bridges in gaps between the g-C_3N_4 layers [37]. For CN, three peaks were observed at 284.8, 286.4 and 288.1 eV in the high-resolution C 1 s spectra; these peaks were assigned to the physically absorbed carbon species or sp^2 C-C bonds, C-NH$_2$ species and typical tri-s-triazine (N-C≡N) in the g-C_3N_4 framework [48,49], respectively (Fig. 2e). Three peaks were found at 398.8, 400.7 and 401.2 eV for high-resolution N 1 s spectra (Fig. 2f). The peak at 398.8 eV could be attributed to the sp^2 hybridised nitrogen (C-N = C group), the 400.7 eV peak corresponded to the tertiary N (C_3-N or C_2-N-H), and the one centred at 401.2 eV was assigned to the amino functional group (C-NH$_x$) in heterocycles [50,51]. However, compared with CN, negligible chemical shifts of C 1 s and N 1 s peaks were observed in the CNN sample, suggesting that the quenching treatment was difficult to induce the change of the surface electronic distribution of g-C_3N_4. Notably, in comparison with CN, two apparent differences could be found in KCNN. The first peak was the increase intensities of peaks located at 284.9 eV,

suggesting the loss of lattice nitrogen and the formation of nitrogen vacancy in KCNN. The second was the increase intensities of peaks located at 286.2 eV, which could be ascribed to the introduction of cyano group, which possesses similar C1s binding energy to C-NHx. Furthermore, the C 1 s and N 1 s peaks of KCNN shift slightly towards higher binding energy than that of CN, suggesting the generation of cyano groups whose N 1 s binding energy were intermediate between those of N_2C and N_3C. In addition, the intensities of N_2C peaks in KCNN spectra apparently decrease, indicating that nitrogen vacancy was successfully formed. Furthermore, elemental analysis (EA) results revealed that C/N atomic ratio for CN was 0.66 (Table S2), while the C/N atomic ratio for KCNN increase to 0.70, suggesting the loss of lattice nitrogen and the formation of nitrogen vacancy in KCNN. EPR spectroscopy was carried out to verify the formation of nitrogen vacancy in KCNN (Fig. S3). In general, CN always has inevitable defects owing to the high-temperature polymerisation reaction [52]. Therefore, bulk CN was used as the standard. The intensity of EPR spectra in CNN was almost unchanged, while an increased EPR signal appeared in KCN and KCNN, which could be ascribed to the few unpaired electrons due to the loss of lattice nitrogen [53]. These results indicated that quenching was unable to form nitrogen vacancies and K^+ doping could induce the formation of nitrogen vacancies, which was consistent with previous literatures.

The photocatalytic performance of the as-prepared samples was evaluated by NO removal in a continuous flow reaction system under LED light irradiation. After achieving NO adsorption–desorption equilibrium on the surface of the samples, the LED lamp was switched on to trigger the photocatalytic reaction. As shown in Fig. 3a, the NO concentration of all samples gradually decreased and held in a state of equilibrium under light irradiation. Thereinto, the CN sample exhibited moderate photocatalytic activity with a NO removal ratio of 38.1%, while the NO removal ratio of CNN sample (54.5%) was higher than that of CN. This phenomenon might be attributed to the existence of hierarchical porous structure and larger specific surface area in CNN, which contributed to the adsorption of reactants (NO, O_2 and water). The KCN sample exhibited a NO removal rate of 58.6%, which was significantly higher than that of CN and CNN samples. After the K doping and the
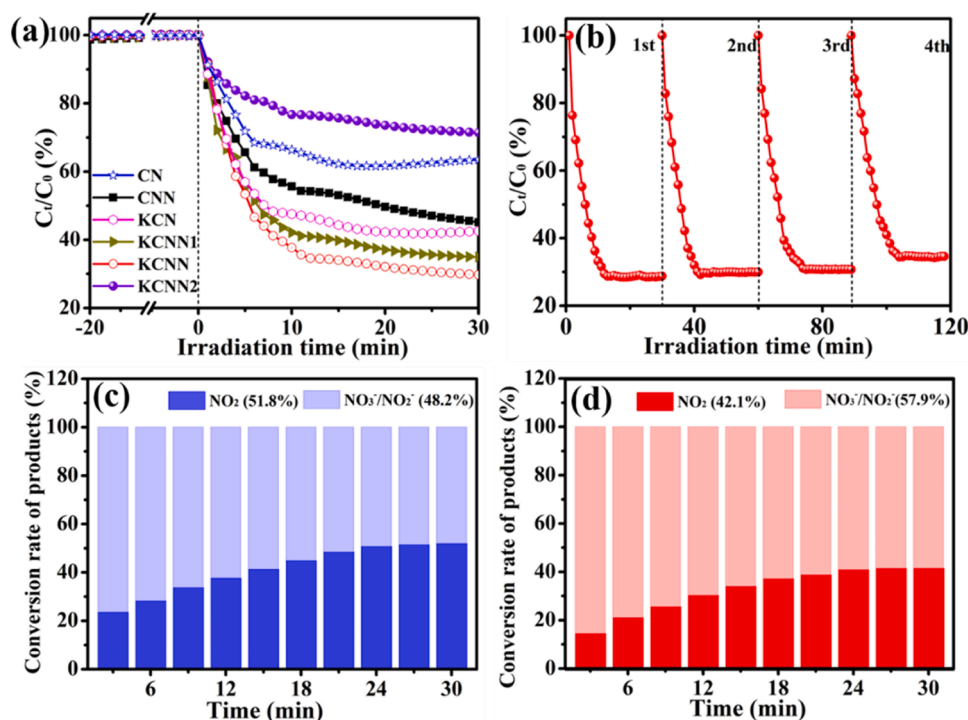

Fig. 3. (a) photocatalytic oxidation efficiencies for NO removal over the as-prepared samples; (b) Cycling test of the KCNN sample; Relative intensity of conversion during 30 min of photocatalytic NO*x* oxidation for (c) CN and (d) KCNN.

quenching treatment, the NO removal rate of KCNN1 and KCNN was significantly enhanced compared with CN and CNN, especially, KCNN reached the highest NO removal rate of 70.5%, while KCNN2 showed the lowest NO removal rate compared with other samples. Therefore, these results testified that the modest amount of K^+ ions doping could improve the photocatalytic activity, and the liquid nitrogen treatment was able to further enhance the NO removal efficiency. The enhancement in photocatalytic performance was explained as follows: on the one hand, the K^+ ions doping adjusted the electron distribution of the in-plane structure of CN, accelerating the charge separation and transfer; On the other hand, the quenching treatment induced a higher specific surface area and hierarchical porous structure, thereby effectively improving the adsorption and active sites. However, the excessive K^+ ions doping caused the aggregation or crystallizing on the surface of the catalyst so that some active sites were blocked, resulting in a decreased photocatalytic activity. In order to detect the NO remove efficiency stability of the catalysts, the photocatalytic experiment was performed under the same conditions. As shown in Fig. 3b, the photocatalytic NO remove rate over KCNN was only slightly decreased after four runs, indicating that the photocatalytic efficiency of NO oxidation over KCNN was acceptably stable. In addition, the XRD analysis before and after the

photocatalytic reaction over KCNN was also studied, and the result exhibited no significant structural change (Fig. S4). This finding confirms the high stability and durability of the catalyst. As we known, the produced intermediate NO_2 is more poisonous than NO during photocatalytic NO oxidation. If NO_2 is not removed by water timely, the secondary pollution to the atmosphere will appear. As shown in Fig. 3c and d, compared with the CN, the production of NO_2 by-product over KCNN was suppressed by 9.7%. This result indicated that the K^+ ion doping and liquid nitrogen treatment not only increased the photoreactivity but also severely retarded the generation of nocuous NO_2 by-product.

The optical properties of the as-prepared samples were investigated by UV−vis diffuse reflectance spectra. As displayed in Fig. 4a, all samples exhibited strong absorption in the visible region. The light absorption band edge of CNN almost kept unchanged compared with that of CN. However, KCN and KCNN showed red shift of the light absorption band edge and enhanced absorbance in the ultraviolet and visible light regions in contrast to CN and CNN, which could be ascribed to the introduction of cyano groups and K^+ ions [54]. Based on the band gap (E_g) of the as-prepared samples estimated from the intercept of the tangents to the plots of $(\alpha h\nu)^{1/2}$ against photo energy (Fig. 4b), the E_g of CN, CNN,
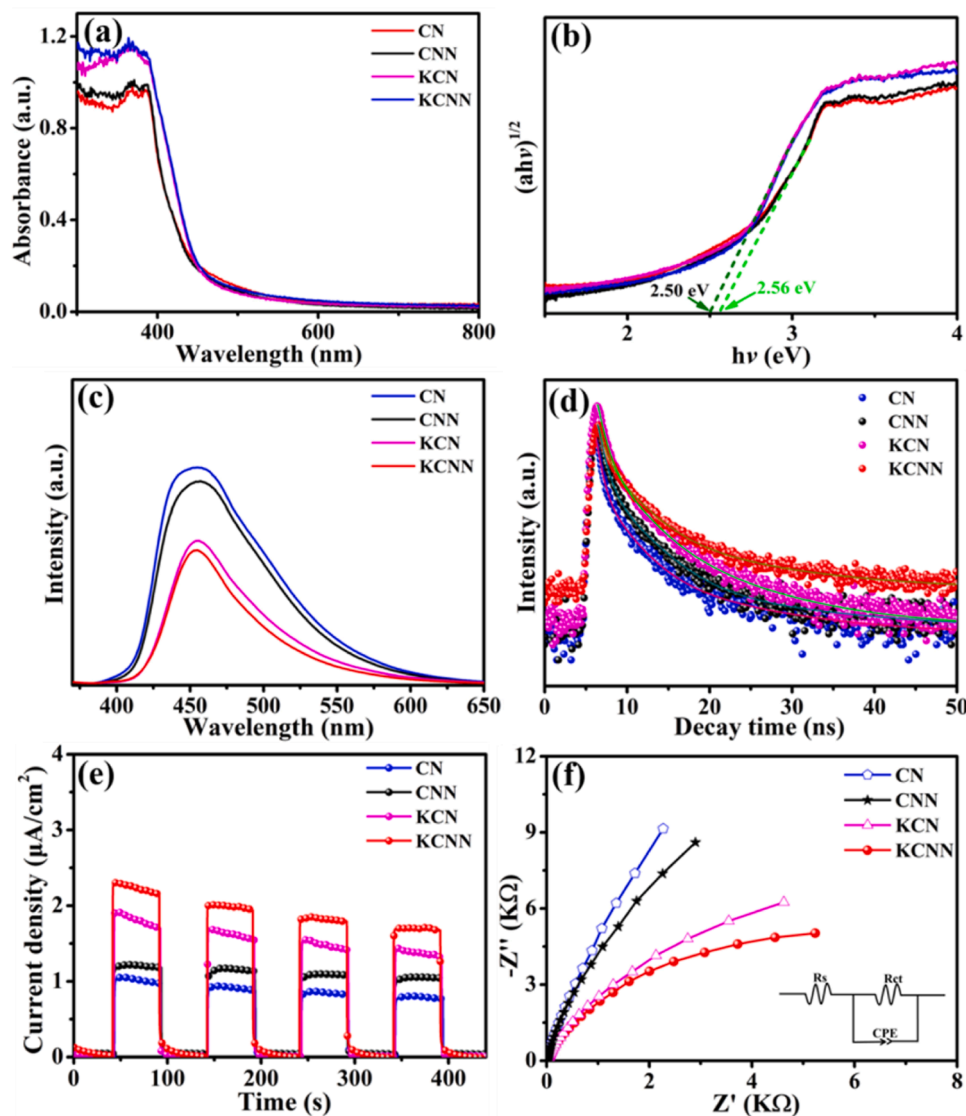
Fig. 4. (a) UV−vis light absorption spectra and (b) plots of $(\alpha h\nu)^{1/2}$ vs $h\nu$ of CN, CNN, KCN and KCNN. (c) Steady-state photoluminescence (PL) spectra, (d) time-resolved fluorescence (TRPL) spectra, (e) transient photocurrent response curves, and (f) electrochemical impedance spectroscopy (EIS) Nyquist plots for CN, CNN, KCN, and KCNN samples.

KCN and KCNN were found to be 2.56, 2.56, 2.50 and 2.50 eV, respectively. The narrower band gap would be conducive to further improve the photocatalytic performance. Besides, the valance band (VB) of the as-prepared samples was revealed by ultraviolet photoelectron spectroscopy (UPS). As shown in Fig. S5a-d, the VB energy (E_{VB}) of CN, CNN, KCN and KCNN were determined to be 5.85, 5.82, 6.11 and 6.07 eV, respectively. The reference standard for which 0 V could be reversible hydrogen electrode (RHE) equals − 4.44 eV vs. vacuum level [55]; thus, the E_{VB} of CN, CNN, KCN and KCNN were estimated to be about 1.41, 1.38, 1.67 and 1.63 V (vs. RHE) respectively. Combined with the E_g measured by UV–vis DRS, the conduction band (CB) was obtained by the following formula (1) [56]:

$$E_{CB} = E_{VB} - E_g \qquad (1)$$

Thus, the positions of the CB edge maxima were estimated to be − 1.15, − 1.18, − 0.83 and − 0.87 eV for CN, CNN, KCN and KCNN, respectively. The band structures of the as-prepared samples were compared in Fig. S6. It was obvious that the introduction of K^+ ions into the CN framework resulted in a negatively shifted CB position. The negative shifted CB potential of KCN and KCNN facilitated the photo-generated electron to transfer from CB to oxygen, leading to the formation of super oxide radicals ($\cdot O_2^-$), which are important reactive oxygen species (ROSs) for NO oxidation. To further unravel the effect of K^+ and N vacancy on electronic properties of g-C₃N₄, the band structures of CN and KCNN were calculated using the models of pristine CN and K-doped CN with N vacancy. As revealed by Fig. S7a and b, the variation trend of E_g upon the introduction of K^+ agrees with the experimental results, in which the E_g of KCNN (0.76 eV) is narrower than that of CN (1.17 eV). The reduction of semiconductor bandgap can improve the light utilization ability of g-C₃N₄, thereby enhancing the photocatalytic performance of NO oxidation. It is noteworthy that the Fermi level of KCNN was uplifted compared to that of CN, suggesting that the doping of K^+ facilitates the escaping the electron from KCNN surface to participate in the photocatalytic NO oxidation. Differential charge density map reveals the charge transfer between K^+ and adjacent N and C atoms (Fig. S7c). K-doped CN with N vacancy showed that the charges were inclined to deplete from K atom (blue isosurface) and accumulate around neighboring N atom in CN layer (yellow isosurface), indicating that the electrons tended to transport from K atom to the CN lattice skeleton, which will effectively promote the separation of charge carriers. The photo-electrochemical characterisations were also performed and the results are shown in Fig. 4c-f. The steady-state photo-luminescence (PL) spectra displayed that the PL intensity of CNN and KCN significantly decreased in comparison to CN (Fig. 4c), which suggested that the quenching treatment and K^+ ions doping could improve separation efficiency of electron-hole. Remarkably, the PL intensity of KCN was lower than that of CNN, which was attributed to the existence of K-derived charge channels, accelerating the charges separation. Compared with CN, CNN and KCN, the KCNN sample showed the lowest PL intensity, which indicated that the synergistic effect of quenching treatment and K doping could further accelerated the separation/migration rate of photoexcited electron-hole. The time-resolved fluorescence (TRPL) spectra are presented in Fig. 4d, a bi-exponential fitting was chosen to analyse the fluorescence decay curves. The fitted parameters, average lifetimes, energy transfer rate and photoluminescence quantum yield are shown in Table S3. In contrast to CN (2.63 ns), the average lifetime of charge carriers was prolonged for CNN (2.91 ns), KCN (3.34 ns) and KCNN (4.19 ns), respectively. The longest τ_{av}, and the optimal energy transfer rate as well as photoluminescence quantum yield have been achieved in KCNN, further elucidating that quenching treatment and K doping could largely suppress the recombination of photogenerated carriers, and the synergistic effect of them ensured more efficient electron separation. Besides, the transient photocurrent responses of the as-prepared samples were carried out by several UV–visible light on-off cycles. As shown in Fig. 4e, the photocurrent density of CNN was higher than that of CN, indicating that the quenching

treatment inducted the higher specific surface area and hierarchical porous structure of g-C₃N₄, leading to the promotion of charge transfer and separation. The photocurrent density of KCN and KCNN was higher than those of CN and CNN, especially KCNN, which showed the highest photocurrent density, indicating the more efficient $e^- - h^+$ pair separation and transfer after the introduction of K^+ ions into the CNN. Furthermore, the results of electrochemical impedance spectra (EIS) are consistent with the photocurrent response (Fig. 4f). The arc diameter in EIS Nyquist plot of KCNN was all smaller than those of CN, CNN and KCN and confirmed that the charge separation and transfer efficiency reached the highest in the KCNN sample. Based on the above results, it can be ascertained that the quenching treatment induces high specific surface area and hierarchical porous structure, and K^+ ions doping constructed the electron transfer channels and defects, which improved the distribution and transfer of electrons in the in-plane structure and adjacent layers, resulting in the superior photocatalytic performance.

To further account for the improvement of NO remove efficiency on KCNN, DFT calculations were performed using the models of CN, K-doped CN and K-doped CN with N vacancy. The optimized structure models of NO adsorption on the surface of them were compared (Fig. 5a-b and Fig. S8). The adsorption energy (E_{ads}) on CN and K-doped CN were relatively low (−0.03 eV and −0.21 eV, respectively), the N-O bond length almost unchanged (1.17 Å and 1.18 Å, respectively). These results indicated that NO molecule was adsorbed weakly on the CN and K-doped CN, and they were mainly physical absorption on the surface of catalyst. Meanwhile, the adsorption of NO on K-doped CN induced the model distortion, which causes K ion to move out of the cell. However, the N vacancy was introduced into the K-doped CN, the NO molecular was spontaneously adsorbed at the N_{2C}-deficient site (E_{ads}=−4.86 eV, and N-O bond length was 1.28 Å), suggesting that the introduction of N vacancy was conducive to the adsorption and activation of NO on the surface of catalyst. Furthermore, the electron transfer (Δq) of CN was calculated to be − 0.012 e; while the Δq of KCNN were 0.867 e, indicating the preferential electron transfer from N vacancy to the adsorbed NO molecules on K-doped CN with N vacancy [57], which were thermodynamically favourable for NO oxidation.

The active radical species played key roles in photocatalytic reaction of NO oxidation. Therefore, active species trapping experiments for KCNN were first carried out to investigate the photocatalytic NO removal mechanism. 4-chloro-2-nitrophenol (4-CHN), 1,4-benzoquinone (BQ), isopropanol (IPA) and potassium iodide (KI) were added into the catalytic system to adopt as the scavengers for singlet oxygen ($^1O_2$), superoxide radical ($\cdot O_2^-$), hydroxyl radicals ($\cdot OH$) and holes (h^+), respectively. As shown in Fig. S9a, by adding BQ, the remove rate of NO decreased by 26.3, demonstrating that $\cdot O_2^-$ was the main active specie for the photocatalytic NO oxidation. When the scavenger 4-CHN and IPA were added, the remove rate of NO decreased by 35.6% and 40.1%, suggesting that $^1O_2$ and $\cdot OH$ also played important roles in the oxidation process. However, the addition of KI resulted in minimal effects on the remove efficiency of NO, indicating that h^+ radical was not the major active species for photooxidation. In order to further prove the existence of singlet oxygen ($^1O_2$) specie, EPR test was carried out. As shown in Fig. S9b, in the presence of TEMP (2,2,6,6-tetramethylpiperidine trapping agent), the characteristic electron paramagnetic resonance (EPR) triplet spectra could be found for TEMP-$^1O_2$ after irradiation for 10 min, confirming the generation of $^1O_2$ during the photocatalytic process. Moreover, to intuitively reveal the conversion pathways and reaction mechanism of NO remove over KCNN sample, in-situ diffused reflectance infrared Fourier transform spectroscopy (DRIFTS) was carried out, and the results are shown in Fig. 6a and b. In the dark, multiple of absorption bands were observed after the injection of NO and O₂ gas in the reaction system (Fig. 6a). A negative peak belonged to OH⁻ stretching vibration at 3550 cm⁻¹ was detected. Meanwhile, some nitrogen-oxide species were also observed with the gradually strengthened peaks of NO⁻/NOH (1145 and 1128 cm⁻¹) and NO₂ (985 cm⁻¹), indicating that the adsorption of NO and disproportionation reaction (3NO + OH⁻ =
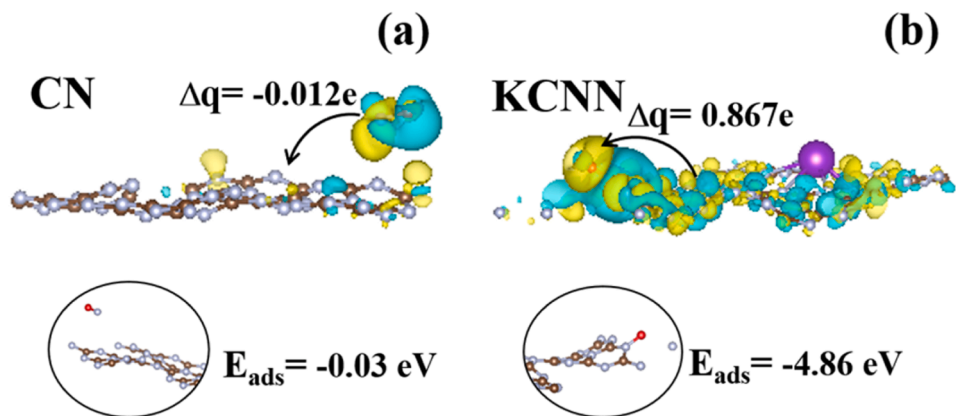
Fig. 5. Side view of the charge density difference of (a) CN and (b) KCNN with adsorbed NO. The charge accumulation is shown in yellow, and the charge depletion is shown in blue.
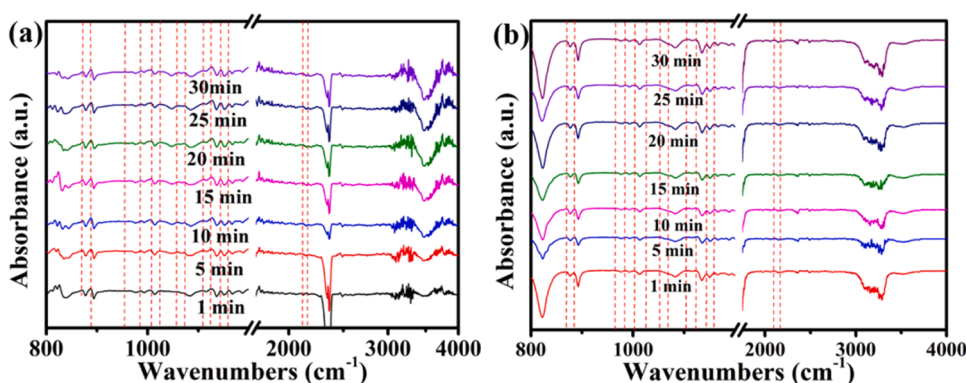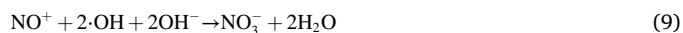

Fig. 6. In-situ DRIFTS recording the (a) adsorption and (b) photocatalytic oxidation of NO over KCNN sample.

$NO_2 + NO^- + NOH$) occur before the light irradiation [58]. Beyond that, a series of infrared peaks appeared assigned to NO_2^- (887, 1019 cm^{-1}) and NO_3^- (870, 991, 1005 cm^{-1}) appeared, such species were crucial intermediates in the NO adsorption process, and were probably derived from the partial electron migration in the 5σ orbit of NO [59]. After the NO adsorption equilibrium was reached and the reaction system was irradiated by LED lamp. The peak intensity of most intermediates, such as N_2O (2165 cm^{-1}), NO_2^- (1109, 1076, 1019, 887 cm^{-1}) and NO_3^- (1056, 1005, 991, 870 cm^{-1}) progressively increases (Fig. 6b), indicating that the reaction between NO and O_2 occurred on the catalyst surface [19]. Moreover, the NO^+ with the peak at 2130 cm^{-1} was detected, suggesting that co-existing of the N vacancies and K^+ ion charge channels in hierarchical porous g-C_3N_4 can facilitate the activation of NO by formation of NO^+ during the irradiation [60], which is beneficial for the deep oxidation of NO into non-toxic products. The peak of N_2O_4 (NO_2) at 964 cm^{-1} was weak and even negligible, which was in accordance with the low evolution rate of NO_2 in Fig. 3d. According to the above characterization analysis and DFT calculations, the photocatalytic reaction mechanism of NO removal was proposed as follows (Eqs. 2–11), aiming to rationalize the enhanced photocatalytic activity for KCNN sample.

$$KCNN + h\nu \rightarrow e^- + h^+ \tag{2}$$

$$NO + \cdot OH \rightarrow NO^+ + OH^- \tag{3}$$

$$NO + \cdot O_2^- + 2e^- + 2H_2O \rightarrow NO^+ + 4OH^- \tag{4}$$

$$2NO + O_2 \rightarrow 2NO_2 \tag{5}$$

$$2NO_2 + \cdot O_2^- + e^- \rightarrow 2NO_3^- \tag{6}$$

$$NO_2 + \cdot OH \rightarrow NO_3^- + H^+ \tag{7}$$

$$NO^+ + \cdot O_2^- + e^- \rightarrow NO_3^- \tag{8}$$

$$NO^+ + 2 \cdot OH + 2OH^- \rightarrow NO_3^- + 2H_2O \tag{9}$$

$$\cdot O_2^- + 2NO + e^- \rightarrow 2NO_2^- \tag{10}$$

$$2NO_2^- + {}^1O_2 \rightarrow 2NO_3^- \tag{11}$$

Based on the above experimental results, characterisations and analyses, photocatalytic NO oxidation on KCNN was proposed. Initially, KCNN was photoexcited to produce electrons (e^-) and holes (h^+) under light irradiation. Upon co-existence of N vacancies and K^+ ions of porous g-C_3N_4, the intrinsic light harvesting capacity and charge carrier separation efficiency were dramatically enhanced, thereby the $\cdot O_2^-$ and $\cdot OH$ radicals were formed by the activation of O_2 ($O_2/\cdot O_2^- = -0.33$ V) and OH^- ($\cdot OH/OH^- = +1.99$ V), respectively [18]. Meanwhile, $^1O_2$ radical was also formed through the oxidation of the superoxide radical by the valence band holes. Under the attack of ROS, the adsorbed NO molecules and intermediates (e.g. NO^+, NO_2^-) were further oxidised. According to the results in Fig. S6, the valence band positions of all samples were not satisfactory to generate $\cdot OH$ radicals, but the active species experiment demonstrated the important role in photocatalytic NO oxidation, which was due to the presence of cyano and hydroxyl groups in the CN framework and the adsorption of O_2 on the surface of catalyst, thus generating $\cdot OH$. In general, NO photocatalytic oxidation can be achieved through two routes: $NO \rightarrow NO_2 \rightarrow NO_3^-$ and $NO \rightarrow NO^+ \rightarrow NO_3^-$.

According to the in-situ DRIFTS results, NO^+ intermediate was detected, thus the route $NO \rightarrow NO^+ \rightarrow NO_3^-$ was preferable on the surface of KCNN sample. Additionally, the NO and intermediates are more easily absorbed at N-vacancies through bidentate states, as shown in Fig. 5; and more ROSs were produced owing to the better separation efficiency of charge carriers on KCNN, Thus, KCNN exhibited better performance in suppressing the formation of toxic intermediates during NO photo-oxidation, compared with bulk CN.

4. Conclusions

A hierarchical porous g-C_3N_4 photocatalyst modified with N vacancies and charge channels (KCNN) was successfully prepared by the thermal polymerisation in KCl medium followed by quenching treatment. The optimised sample KCNN exhibits a large photoreactivity improvement, with a NO removal rate of 70.5%, which was superior to bulk g-C_3N_4 (38.1%), porous g-C_3N_4 (54.5%) and K-doped g-C_3N_4 (58.6%), respectively. The synergy of hierarchical porous structure, N vacancy and K^+ ions improved the photocatalytic NO purification and suppressed NO_2 emission through a combination of increased surface area, extended optical absorption, promoted electron excitation/transfer and subsequent enlarged ROS production. Moreover, in-situ DRIFTS revealed the photo-oxidation mechanism of NO on KCNN through a preferred pathway ($NO \rightarrow NO^+ \rightarrow NO_3^-$). This study demonstrates the possibility to integrate ion doping and vacancy engineering to boost the photocatalytic activity of g-C_3N_4 towards NO_x degradation.

CRediT authorship contribution statement

Yang Xia: Conceptualization, Data curation, Formal analysis, Investigation, Methodology, Writing – original draft. **Heng Yang**: Data curation, Formal analysis, Investigation. **Wingkei Ho**: Conceptualization, Funding acquisition, Methodology, Supervision, Writing – review & editing. **Bicheng Zhu**: Data curation, Formal analysis, Investigation. **Jiaguo Yu**: Conceptualization, Funding acquisition, Supervision, Writing – review & editing.

Declaration of Competing Interest

The authors declare that they have no known competing financial interests or personal relationships that could have appeared to influence the work reported in this paper.

Data Availability

Data will be made available on request.

Acknowledgements

Appendix A. Supporting information

Supplementary data associated with this article can be found in the online version at doi:10.1016/j.apcatb.2023.123604.

References

[1] J. Zhu, B. Yang, Y. Deng, M. Chen, H. Wang, A. Wang, W. Gao, J. She, M. Luo, Y. Liu, Z. Fu, A mild and effective photo-catalytic protocol for triggering inert nitrous oxide to participate in oxidative dehydrogenation of alcohols under visible light illumination, Appl. Catal. B: Environ. 318 (2022), 121861.

[2] N. Li, C. Wang, K. Zhang, H. Lv, M. Yuan, D.W. Bahnemann, Progress and prospects of photocatalytic conversion of low-concentration NOx, Chin. J. Catal. 43 (2022) 2363–2387.

[3] C. Ma, J. Wei, K. Jiang, J. Chen, Z. Yang, X. Yang, G. Yu, C. Zhang, X. Li, Typical layered structure bismuth-based photocatalysts for photocatalytic nitrogen oxides oxidation, Sci. Total Environ. 855 (2023), 158644.

[4] A. Talaiekhozani, S. Rezania, K.-H. Kim, R. Sanaye, A.M. Amani, Recent advances in photocatalytic removal of organic and inorganic pollutants in air, J. Clean. Prod. 278 (2021), 123895.

[5] J. Lasek, Y.-H. Yu, J.C. Wu, Removal of NOx by photocatalytic processes, J. Photoch. Photobio. C. 14 (2013) 29–52.

[6] Y. Yang, T. Ji, Y. Lin, W. Su, Effect of adhesive on photocatalytic NOx removal and stability over polymeric carbon nitride coated cement mortars, J. Clean. Prod. 295 (2021), 126458.

[7] H. Wang, K. Li, J. Li, Y. Sun, F. Dong, Photochemical transformation pathways of nitrates from photocatalytic NOx oxidation: Implications for controlling secondary pollutants, Environ. Sci. Technol. Lett. 8 (2021) 873–877.

[8] V.-H. Nguyen, B.-S. Nguyen, C.-W. Huang, T.-T. Le, C.C. Nguyen, T.T.N. Le, D. Heo, Q.V. Ly, Q.T. Trinh, M. Shokouhimehr, Photocatalytic NOx abatement: Recent advances and emerging trends in the development of photocatalysts, J. Clean. Prod. 270 (2020), 121912.

[9] Y.G. Adewuyi, N.E. Khan, Modeling the ultrasonic cavitation-enhanced removal of nitrogen oxide in a bubble column reactor, AIChE J. 58 (2012) 2397–2411.

[10] D. Li, P. Shi, J. Wang, J. Li, R. Su, High-efficiency absorption of high NOx concentration in water or PEG using capillary pneumatic nebulizer packed with an expanded graphite filter, Chem. Eng. J. 237 (2014) 8–15.

[11] M. Pavlovich, T. Ono, C. Galleher, B. Curtis, D. Clark, Z. Machala, D. Graves, Air spark-like plasma source for antimicrobial NOx generation, J. Phys. D: Appl. Phys. 47 (2014), 505202.

[12] R.G. Tonkyn, S.E. Barlow, J.W. Hoard, Reduction of NOx in synthetic diesel exhaust via two-step plasma-catalysis treatment, Appl. Catal. B: Environ. 40 (2003) 207–217.

[13] K. Masera, A.K. Hossain, Modified selective non-catalytic reduction system to reduce NOx gas emission in biodiesel powered engines, Fuel 298 (2021), 120826.

[14] W. Shan, F. Liu, H. He, X. Shi, C. Zhang, A superior Ce-W-Ti mixed oxide catalyst for the selective catalytic reduction of NOx with NH3, Appl. Catal. B: Environ. 115 (2012) 100–106.

[15] X. Qin, H. Tan, Y. Zhao, S. Cheng, M. Zhou, J. Lin, W.-K. Ho, H. Li, S.-C. Lee, Light-emitting diode visible-light-driven photocatalytic redox reactions in nitrogen oxide removal using β-Bi₂O₃/Bi/g-C₃N₄ prepared by one-step in-situ thermal reduction synthesis, Adv. Energy Sustain. Res 4 (2022) 2200157.

[16] M. Ran, J. Li, W. Cui, Y. Li, P. Li, F. Dong, Efficient and stable photocatalytic NO removal on C self-doped g-C₃N₄: Electronic structure and reaction mechanism, Catal. Sci. Technol. 8 (2018) 3387–3394.

[17] M. Zhou, L. Zeng, R. Li, C. Yang, X. Qin, W. Ho, X. Wang, Poly(heptazine imide) with enlarged interlayers spacing for efficient photocatalytic NO decomposition, Appl. Catal. B: Environ. 317 (2022), 121719.

[18] Z. Hu, K. Li, X. Wu, N. Wang, X. Li, Q. Li, L. Li, K. Lv, Dramatic promotion of visible-light photoreactivity of TiO₂ hollow microspheres towards NO oxidation by introduction of oxygen vacancy, Appl. Catal. B: Environ. 256 (2019), 117860.

[19] Z. Hu, Z. Liu, N. Kang, K. Lv, Q. Li, Effect of organic solvents on in-situ growth of defective TiO₂ from Ti₃C₂T MXene nanosheets for photocatalytic NO abatement, Appl. Surf. Sci. 627 (2023), 157324.

[20] Z. Gu, Z. Cui, Z. Wang, K.S. Qin, Y. Asakura, T. Hasegawa, S. Tsukuda, K. Hongo, R. Maezono, S. Yin, Carbon vacancies and hydroxyls in graphitic carbon nitride: Promoted photocatalytic NO removal activity and mechanism, Appl. Catal. B: Environ. 279 (2020), 119376.

[21] X. Xia, C. Xie, Q. Che, P. Yang, Potassium-derived charge channels in boron-doped g-C₃N₄ nanosheets for photocatalytic NO oxidation and hydrogen evolution, Langmuir 39 (2023) 1250–1261.

[22] H. Ma, Y. He, X. Li, J. Sheng, J. Li, F. Dong, Y. Sun, In situ loading of MoO₃ clusters on ultrathin Bi₂MoO₆ nanosheets for synergistically enhanced photocatalytic NO abatement, Appl. Catal. B: Environ. 292 (2021), 120159.

[23] W.C. Huo, J.Y. Li, M. Liu, X.Y. Liu, Y.X. Zhang, F. Dong, Synthesis of Bi₂WO₆ with gradient oxygen vacancies for highly photocatalytic NO oxidation and mechanism study, Chem. Eng. J. 361 (2019) 129–138.

[24] S. Jin, G. Dong, J. Luo, F. Ma, C. Wang, Improved photocatalytic NO removal activity of SrTiO₃ by using SrCO₃ as a new co-catalyst, Appl. Catal. B: Environ. 227 (2018) 24–34.

[25] H. Ma, W. Yang, H. Tang, Y. Pan, W. Li, R. Fang, Y. Shen, F. Dong, Enhance the stability of oxygen vacancies in SrTiO₃ via metallic Ag modification for efficient and durable photocatalytic NO abatement, J. Hazard. Mater. 452 (2023), 131269.

[26] Y. Li, W. Ho, K. Lv, B. Zhu, S.C. Lee, Carbon vacancy-induced enhancement of the visible light-driven photocatalytic oxidation of NO over g-C₃N₄ nanosheets, Appl. Surf. Sci. 430 (2018) 380–389.

[27] B. Xie, D. Chen, N. Li, Q. Xu, H. Li, J. He, J. Lu, Fabrication of an FAPbBr₃/g-C₃N₄ heterojunction to enhance NO removal efficiency under visible-light irradiation, Chem. Eng. J. 430 (2022), 132968.

[28] M. Zhou, G. Dong, F. Yu, Y. Huang, The deep oxidation of NO was realized by Sr multi-site doped g-C₃N₄ via photocatalytic method, Appl. Catal. B: Environ. 256 (2019), 117825.

[29] Y. Ren, Y. Li, X. Wu, J. Wang, G. Zhang, S-scheme Sb₂WO₆/g-C₃N₄ photocatalysts with enhanced visible-light-induced photocatalytic NO oxidation performance, Chin. J. Catal. 42 (2021) 69–77.

[30] G. Liu, Y. Huang, H. Lv, H. Wang, Y. Zeng, M. Yuan, Q. Meng, C. Wang, Confining single-atom Pd on g-C₃N₄ with carbon vacancies towards enhanced photocatalytic NO conversion, Appl. Catal. B: Environ. 284 (2021), 119683.

[31] H. Wang, W. He, X. Dong, G. Jiang, Y. Zhang, Y. Sun, F. Dong, In situ DRIFT investigation on the photocatalytic NO oxidation mechanism with thermally exfoliated porous g-C₃N₄ nanosheets, RSC Adv. 7 (2017) 19280–19287.

[32] D. Zhang, Y. Guo, Z. Zhao, Porous defect-modified graphitic carbon nitride via a facile one-step approach with significantly enhanced photocatalytic hydrogen evolution under visible light irradiation, Appl. Catal. B: Environ. 226 (2018) 1–9.

[33] T. Xiong, H. Wang, Y. Zhou, Y. Sun, W. Cen, H. Huang, Y. Zhang, F. Dong, KCl-mediated dual electronic channels in layered gC 3 N 4 for enhanced visible light photocatalytic NO removal, Nanoscale 10 (2018) 8066–8074.

[34] Y. Wang, C. Li, S. Wan, C. Zhang, Z. Li, S. Zhang, Q. Zhong, ZIF-67-derived ultrathin Co-Ni layered double hydroxides wrapped on 3D g-C₃N₄ with enhanced visible-light photocatalytic performance for greenhouse gas CO₂ reduction, J. Environ. Chem. Eng. 10 (2022), 108119.

[35] L. Yang, J. Huang, L. Shi, L. Cao, Q. Yu, Y. Jie, J. Fei, H. Ouyang, J. Ye, A surface modification resultant thermally oxidized porous g-C₃N₄ with enhanced photocatalytic hydrogen production, Appl. Catal. B: Environ. 204 (2017) 335–345.

[36] Y. Xia, B. Zhu, X. Qin, W. Ho, J. Yu, Zinc porphyrin/g-C₃N₄ S-scheme photocatalyst for efficient H₂O₂ production, Chem. Eng. J. 467 (2023), 143528.

[37] S. Wang, J. Zhan, K. Chen, A. Ali, L. Zeng, H. Zhao, W. Hu, L. Zhu, X. Xu, Potassium-doped g-C₃N₄ achieving efficient visible light driven CO₂ reduction, ACS Sustain. Chem. Eng. 8 (2020) 8214–8222.

[38] B. Liu, L. Yan, J. Wang, Liquid N₂ quenching induced oxygen defects and surface distortion in TiO₂ and the effect on the photocatalysis of methylene blue and acetone, Appl. Surf. Sci. 494 (2019) 266–274.

[39] W. He, L. Liu, T. Ma, H. Han, J. Zhu, Y. Liu, Z. Fang, Z. Yang, K. Guo, Controllable morphology CoFe₂O₄/g-C₃N₄ p-n heterojunction photocatalysts with built-in electric field enhance photocatalytic performance, Appl. Catal. B: Environ. 306 (2022), 121107.

[40] W. Li, Z. Wei, K. Zhu, W. Wei, J. Yang, J. Jing, D.L. Phillips, Y. Zhu, Nitrogen-defect induced trap states steering electron-hole migration in graphite carbon nitride, Appl. Catal. B: Environ. 306 (2022), 121142.

[41] L. Wang, X. Fei, L. Zhang, J. Yu, B. Cheng, Y. Ma, Solar fuel generation over nature-inspired recyclable TiO₂/g-C₃N₄ S-scheme hierarchical thin-film photocatalyst, J. Mater. Sci. Technol. 112 (2022) 1–10.

[42] J. Geng, L. Zhao, M. Wang, G. Dong, W. Ho, The photocatalytic NO-removal activity of g-C₃N₄ significantly enhanced by the synergistic effect of Pd⁰ nanoparticles and N vacancies, Environ. Sci.: Nano 9 (2022) 742–750.

[43] Z. Wang, Q. Wei, N. Zhang, X. Shi, M. Chen, Y. Huang, J. Cao, H. Li, W. Ho, S. Lee, Simultaneous polarization engineering and selectivity regulation achieved using polymeric carbon nitride for promoting NOx photo-oxidation, Appl. Catal. B: Environ. 330 (2023), 122582.

[44] Y. Xia, K. Xiao, B. Cheng, J. Yu, L. Jiang, M. Antonietti, S. Cao, Improving artificial photosynthesis over carbon nitride by gas–liquid–solid interface management for full light-induced CO₂ reduction to C1 and C2 fuels and O₂, ChemSusChem 13 (2020) 1730–1734.

[45] D.E.K. Sing, R. Haul, L. Moscou, Reporting physisorption data for gassolid systems with special reference to the determination of surface area and porosity, Pure Appl. Chem. 57 (1985) 603–619.

[46] M. Kruk, M. Jaroniec, Gas Adsorption characterization of ordered organic-inorganic nanocomposite materials, Chem. Mater. 13 (2001) 3169–3183.

[47] Y. Wang, S. Zhao, Y. Zhang, J. Fang, Y. Zhou, S. Yuan, C. Zhang, W. Chen, One-pot synthesis of K-doped g-C₃N₄ nanosheets with enhanced photocatalytic hydrogen production under visible-light irradiation, Appl. Surf. Sci. 440 (2018) 258–265.

[48] Y. Zheng, Z. Yu, H. Ou, A.M. Asiri, Y. Chen, X. Wang, Black phosphorus and polymeric carbon nitride heterostructure for photoinduced molecular oxygen activation, Adv. Funct. Mater. 28 (2018) 1705407.

[49] P. Xia, S. Cao, B. Zhu, M. Liu, M. Shi, J. Yu, Y. Zhang, Designing a 0D/2D S-scheme heterojunction over polymeric carbon nitride for visible light photocatalytic inactivation of bacteria, Angew. Chem. Int. Ed. 59 (2020) 5218–5225.

[50] J. Wang, G. Wang, B. Cheng, J. Yu, J. Fan, Sulfur-doped g-C₃N₄/TiO₂ S-scheme heterojunction photocatalyst for Congo Red photodegradation, Chin. J. Catal. 42 (2021) 56–68.

[51] L. Lin, H. Ou, Y. Zhang, X. Wang, Tri-s-triazine-based crystalline graphitic carbon nitrides for highly efficient hydrogen evolution photocatalysis, ACS Catal. 6 (2016) 3921–3931.

[52] L. Chen, D. Zhu, J. Li, X. Wang, J. Zhu, P.S. Francis, Y. Zheng, Sulfur and potassium co-doped graphitic carbon nitride for highly enhanced photocatalytic hydrogen evolution, Appl. Catal. B: Environ. 273 (2020), 119050.

[53] H. Zhang, L. Jia, P. Wu, R. Xu, J. He, W. Jiang, Improved H₂O₂ photogeneration by KOH-doped g-C₃N₄ under visible light irradiation due to synergistic effect of N defects and K modification, Appl. Surf. Sci. 527 (2020), 146584.

[54] J. Yang, Y. Liang, K. Li, G. Yang, K. Wang, R. Xu, X. Xie, Cyano and potassium-rich g-C₃N₄ hollow tubes for efficient visible-light-driven hydrogen evolution, Catal. Sci. Technol. 9 (2019) 3342–3346.

[55] Y. Shi, J. Chen, Z. Mao, B.D. Fahlman, D. Wang, Construction of Z-scheme heterostructure with enhanced photocatalytic H₂ evolution for g-C₃N₄ nanosheets via loading porous silicon, J. Catal. 356 (2017) 22–31.

[56] Y. Xia, B. Cheng, J. Fan, J. Yu, G. Liu, Unraveling photoexcited charge transfer pathway and process of CdS/graphene nanoribbon composites toward visible-light photocatalytic hydrogen evolution, Small 15 (2019) 1902459.

[57] P. Zhu, X. Yin, X. Gao, G. Dong, J. Xu, C. Wang, Enhanced photocatalytic NO removal and toxic NO₂ production inhibition over ZIF-8-derived ZnO nanoparticles with controllable amount of oxygen vacancies, Chin. J. Catal. 42 (2021) 175–183.

[58] K. Li, W. Zhou, X. Li, Q. Li, S.A.C. Carabineiro, S. Zhang, J. Fan, K. Lv, Synergistic effect of cyano defects and CaCO₃ in graphitic carbon nitride nanosheets for efficient visible-light-driven photocatalytic NO removal, J. Hazard. Mater. 442 (2023), 130040.

[59] G. Cheng, X. Liu, X. Song, X. Chen, W. Dai, R. Yuan, X. Fu, Visible-light-driven deep oxidation of NO over Fe doped TiO₂ catalyst: Synergic effect of Fe and oxygen vacancies, Appl. Catal. B: Environ. 277 (2020) 119196.

[60] H. Ma, Y. He, J. Sheng, S. Chen, F. Dong, G. Xie, Y. Sun, Doping and facet effects synergistically mediated interfacial reaction mechanism and selectivity in photocatalytic NO abatement, J. Colloid Interface Sci. 604 (2021) 624–634.